

**1      Estimating  $\chi$  using fast-response thermistors on traditional shipboard**

**2      CTDs: sources of uncertainty and bias.**

**3      Andy Pickering\***

**4      College of Earth, Ocean, and Atmospheric Sciences, Oregon State University, Corvallis, OR.**

**5      Jonathan Nash**

**6      College of Earth, Ocean, and Atmospheric Sciences, Oregon State University, Corvallis, OR.**

**7      James N Moum**

**8      College of Earth, Ocean, and Atmospheric Sciences, Oregon State University, Corvallis, OR.**

**9      Jennifer MacKinnon**

**10     UCSD / Scripps Institute of Oceanography**

**11     \*Corresponding author address:** College of Earth, Ocean, and Atmospheric Sciences, Oregon State  
University, Corvallis, OR.

**13     E-mail:** apickering@coas.oregonstate.edu

## ABSTRACT

14 The acquisition of turbulence data from shipboard CTD profiles is attrac-  
15 tive, as it has the potential to significantly increase the amount of deep-ocean  
16 mixing observations globally. While data from shear-probes are easily con-  
17 taminated by motion of the instrument platform, the measurement of temper-  
18 ature gradient is relatively insensitive to vehicle vibration, making it possible  
19 to measure temperature gradient from a shipboard CTD rosette. The purpose  
20 of this note is to investigate the error and bias in estimating the rate of dissi-  
21 pation of temperature variance  $\chi$  from fast thermistors mounted on traditional  
22 CTD casts. The most significant source of error is associated with the fact  
23 that fast-response FP07 thermistors resolve only a fraction of the temperature  
24 gradient variance at the fallspeed of typical CTD casts. Assumptions must  
25 be made about the wavenumber extent of the temperature gradient spectrum,  
26 which scales with the rate of dissipation of turbulent kinetic energy, a quantity  
27 that is not directly measured. Here we utilize observations from a microstruc-  
28 ture profiler with shear probes to demonstrate the validity of our method of  
29 estimating  $\chi$  from thermistor data, and to assess uncertainty and bias. We then  
30 apply this methodology to temperature gradient profiles obtained from  $\chi$ pods  
31 mounted on a CTD (the CTD- $\chi$ pod), and compare these to microstructure  
32 profiles obtained almost synoptically at the equator. CTD- $\chi$ pod estimates  
33 of  $\chi$  compare favorably to the shear-probe microstructure measurements and  
34 demonstrate that the  $\chi$ pod method is not significantly biased. This supports  
35 the utility of the measurement as part of the global repeat hydrography pro-  
36 gram (GO-SHIP) cruises, during which this type of data has been acquired  
37 during the past few years.

<sup>38</sup> **1. Introduction**

<sup>39</sup> Turbulent mixing affects the distribution of heat, salt, and nutrients throughout the global ocean.

<sup>40</sup> Diapycnal mixing of cold, dense water with warmer water above maintains the abyssal overturning

<sup>41</sup> circulation (Munk 1966; Munk and Wunsch 1998), which affects global climate. Because the

<sup>42</sup> turbulence that drives mixing generally occurs at scales that are not resolved in climate models,

<sup>43</sup> it must be parameterized, based on either (i) aspects of the resolved model dynamics, (ii) through

<sup>44</sup> higher resolution models that capture the dynamics that feed energy to turbulence, or (iii) using

<sup>45</sup> other parameterizations that either dynamically or statistically quantify turbulent fluxes. Recent

<sup>46</sup> investigations have demonstrated that these models are sensitive to the magnitude and distribution

<sup>47</sup> of mixing (Melet et al. 2013). A comprehensive set of measurements that spans relevant dynamical

<sup>48</sup> regimes is needed to constrain mixing and develop more accurate parameterizations.

<sup>49</sup> To quantify turbulence, typically either the dissipation rate of turbulent kinetic energy  $\varepsilon$  or the

<sup>50</sup> dissipation rate of temperature variance  $\chi$  are measured. The dissipation rate of TKE may be dy-

<sup>51</sup> namically interesting to internal wave energetics globally, since the energy flow can be tracked and

<sup>52</sup> then  $\varepsilon$  can be used to estimate the potential for mixing. The dissipation rate of temperature vari-

<sup>53</sup> ance  $\chi$  is one of the most easily measured direct metrics of mixing, through  $K_T$ . These quantities

<sup>54</sup> ( $\varepsilon$  and  $\chi$ ) are typically computed by measuring the variance of velocity gradient or temperature

<sup>55</sup> gradient, which have universal theoretical forms with subranges described by power-law formula-

<sup>56</sup> tions (Figure 1). The wavenumber extent and amplitude of the theoretical shear spectrum scales

<sup>57</sup> with  $\varepsilon$ . In contrast, the temperature gradient spectrum amplitude scales with both  $\chi$  and  $\varepsilon$ , and

<sup>58</sup> the wavenumber extent scales with  $\varepsilon$ .

<sup>59</sup> The most accurate measurements of turbulence are made with microstructure profilers equipped

<sup>60</sup> with shear probes. Shear probes are used to measure the spectra of velocity shear at small enough

scales that a fit to standard inertial subrange spectral shapes allows an estimate of the turbulent dissipation rate ( $\varepsilon$ ) as a fitting parameter. This technique is well-suited for targeting upper-ocean processes, but can be expensive, time-intensive, and requires considerable care and expertise. Moreover, tethered profilers can't reach abyssal depths, requiring autonomous instruments to get deeper than  $\sim$ 1000-2000 m. As a result, existing measurements of diapycnal mixing, especially in the deep ocean, are sparse (Waterhouse et al. 2014). In order to obtain a larger quantity of mixing estimates, considerable work has gone into inferring mixing from measurements of the outer scales of turbulence, which are easier to obtain. One popular method is the use of Thorpe scales, where diapycnal mixing is inferred from inversions in profiles of temperature or density (Thorpe 1977; Dillon 1982). The size of resolvable overturn is limited by the profiling speed and instrument noise (Galbraith and Kelley 1996). While some studies indicate relatively good agreement with microstructure and other observations, there remain questions about the general validity of the method and the assumptions made (Mater et al. 2015; Scotti 2015). Parameterizations based on profiles of shear and/or strain have also been developed and applied to estimate diapycnal mixing (Gregg 1989; Kunze et al. 2006; Polzin et al. 2014; Whalen et al. 2012, 2015). However, they rely on a series of assumptions about the cascade of energy from large to small scales (they assume turbulence rates are set by an energy cascade through the internal wave field) that are often violated; numerous studies (i.e., Waterman et al. (2013)) have shown that there is significant uncertainty associated with these parameterizations, in that there can be a consistent bias in a particular region, yet the sense of the bias (i.e., over-predict vs. under-predict) is not known a priori.

Quantifying turbulence from velocity shear variance (to compute the dissipation rate of turbulent kinetic energy  $\varepsilon$ ) is challenging on moorings or profiling platforms because there is usually too much vibration and/or package motion for shear-probes to be useful. Pitot-static tubes have recently been used for this purpose, plus providing independent measurements of speed (Moum

2015). Other methods (i.e., optics or acoustics) may hold some promise, but lack of scatterers often precludes this type of measurement, especially in the abyss. In addition, shear probes only provide  $\varepsilon$ , not the diapycnal diffusivity of scalars,  $K$ , which is often inferred from  $\varepsilon$  by assuming a mixing efficiency  $\Gamma$  (Osborn 1980) as  $K = \Gamma\varepsilon/N^2$ , where  $N^2$  is the buoyancy frequency. A more direct measure of turbulent mixing is obtained from the dissipation rate of temperature variance  $\chi$  (Osborn and Cox 1972). This has the advantage that (i) the temperature and temperature gradient can be computed and are relatively straightforward to measure, and (ii) the estimation of mixing from  $\chi$  does not require assumptions about  $\Gamma$ . However, the spectrum of temperature gradient extends to very small scales, so that its spectrum is seldom fully resolved (and unlike shear variance, the wavenumber extent of the temperature gradient spectrum does not scale with its amplitude, but instead depends on  $\varepsilon$  (Figure 1). Assumptions about the spectral shape (Kraichnan vs. Batchelor, and the value of the “constant”  $q$ ) and its wavenumber extent (governed by the Batchelor wavenumber  $k_b = [\varepsilon/(vD_T^2)]^{1/4}$  (Batchelor 1959)) are thus necessary to determine  $\chi$  unless measurements capture the full viscous-diffusive subrange of turbulence (i.e., down to scales  $\Delta x \sim 1/k_b \sim 1\text{mm}$ ), a criterion seldom achieved. To resolve this, we follow Alford and Pinkel (2000) and Moum and Nash (2009) and make the assumption that  $K_T = K_\rho$  to determine the dissipation rate as  $\varepsilon_\chi = (N^2\chi)/(2\Gamma < dT/dz >^2)$ , permitting estimation of  $k_b$ .

The goal of this paper is to outline and validate the methods used to compute  $\chi$  and  $K_T$  with  $\chi$ pods mounted on CTDs (Figure 2). We do this by applying our processing methodology to profiles of temperature gradient measured by thermistors on the ‘Chameleon’ microstructure profiler, which provides a direct test of our methodology. Because Chameleon is a loosely tethered profiler equipped with shear probes (Moum et al. 1995), it directly measures  $\varepsilon$  and allows us to test our assumptions. Specifically, it allows us to determine biases associated with computing  $\chi$  from partially-resolved temperature gradient spectra alone, as compared to computation that includes  $\varepsilon$ ,

<sup>109</sup> which constrains the wavenumber extent of the scalar spectra. After establishing that the method  
<sup>110</sup> works, we then compare CTD- $\chi$ pod profiles to nearby microstructure profiles.

<sup>111</sup> **2. Data**

<sup>112</sup> *a. EQ14*

<sup>113</sup> Data were collected on the R/V Oceanus in Fall 2014 during the EQ14 experiment to study  
<sup>114</sup> equatorial mixing. More than 2700 Chameleon profiles were made, along with 35 CTD- $\chi$ pod  
<sup>115</sup> profiles bracketed by Chameleon profiles in order to maintain calibrations during the cruise. Most  
<sup>116</sup> Chameleon profiles were made to a maximum depth of about 250m, with CTD casts going to  
<sup>117</sup> 500m or deeper. The EQ14 experiment and results are discussed in more detail in ( SJ Warner, RN  
<sup>118</sup> Holmes, EH McHugh-Hawkins, JN Moum, 2016: Buoyant gravity currents released from tropical  
<sup>119</sup> instability waves, JPO, in preparation) and Holmes et al. (2016).

<sup>120</sup> **3. Methods**

<sup>121</sup> As mentioned in the introduction, the temperature gradient spectrum is rarely fully resolved  
<sup>122</sup> down to the small scales of turbulent mixing. The fraction of the spectrum resolved depends on  
<sup>123</sup> the true spectrum (a function of  $\chi$  and  $\varepsilon$ ), the flowspeed past the sensor ( $u$ ), and the response of  
<sup>124</sup> the thermistor. The GE/Thermometrics FP07 thermistors we use typically resolve frequencies up  
<sup>125</sup> to about  $f_{max} = 10 - 15$  Hz. The maximum resolved wavenumber is then equal to  $k_{max} = f_{max}/u$ ,  
<sup>126</sup> while the wavenumber extent of the true spectrum varies with  $k_b$  (and  $\varepsilon^{1/4}$ ). At the typical vertical  
<sup>127</sup> fall rate of a CTD rosette ( $\sim 1$ m/s), only about 20% of  $k_b$  is resolved at  $\varepsilon = 10^{-10} W kg^{-1}$  (Figure  
<sup>128</sup> 3). While methods have been developed to fit the observed temperature gradient spectrum to  
<sup>129</sup> theoretical forms (Ruddick et al. 2000), these work only when a larger fraction of the temperature  
<sup>130</sup> gradient spectrum is resolved. For the relatively high profiling speeds typical of CTD casts, we

<sup>131</sup> find these methods do not work well (see appendix for more details) and therefore we use the  
<sup>132</sup> following methodology, which does not have a strongly  $\varepsilon$ -dependent bias.

<sup>133</sup> We first outline our method for estimating  $\chi$ , which relies on (i) determining the instantaneous  
<sup>134</sup> flowspeed past the sensor, (ii) identifying periods where the signals may be contaminated by the  
<sup>135</sup> wake of the CTD rosette, (iii) defining the relevant values of  $N^2$  and  $(dT/dz)^2$ , and (iv) applying  
<sup>136</sup> an iterative method to compute  $\chi$ . We then discuss some limitations and practical considerations  
<sup>137</sup> that arise.

<sup>138</sup> *a. Iterative Method for estimating  $\chi$*

<sup>139</sup> For each  $\sim 1$  second window,  $\chi$  is estimated via the following procedure as outlined in Moum  
<sup>140</sup> and Nash (2009). For isotropic turbulence,

$$\chi_T = 6D_T \int_0^\infty \Psi_{T_x}(k) dk \quad (1)$$

<sup>141</sup> where  $D_T$  is the thermal diffusivity and  $\Psi_{T_x}(k)$  is the wavenumber spectrum of  $dT/dx$ .

<sup>142</sup> Note that  $dT/dx$  is not actually measured;  $dT/dt$  is measured, and  $dT/dx$  is inferred from  
<sup>143</sup> Taylor's frozen flow hypothesis:

$$\frac{dT}{dx} = \frac{1}{u} \frac{dT}{dt} \quad (2)$$

<sup>144</sup> where  $u$  represents the flow speed past the sensor. The wavenumber extent of the spectrum depends  
<sup>145</sup> on the Batchelor wavenumber  $k_b$ , which is related to  $\varepsilon$ :

$$k_b = [\varepsilon/(vD_T^2)]^{1/4} \quad (3)$$

<sup>146</sup> We assume that  $K_\rho = K_T$  and  $K_\rho = \Gamma\varepsilon/N^2$  where the mixing efficiency  $\Gamma$  is assumed to be 0.2  
<sup>147</sup> (Moum and Nash 2009). Then dissipation rate is computed as

$$\varepsilon_\chi = \frac{N^2 \chi_T}{2\Gamma \langle dT/dz \rangle^2} \quad (4)$$

148 Typical thermistors do not resolve the spectrum out to  $k_b$ , so the measured spectrum is fit to  
 149 the Kraichnan form (with  $q = 7$ ) of the theoretical scalar spectrum over the range of resolved  
 150 wavenumbers ( $k_{min} < k < k_{max}$ ). The variance between the measured  $[\Phi_{T_x}(k)]_{obs}$  and theoretical  
 151  $[\Phi_{T_x}(k)]_{theory}$  spectra at these wavenumbers is assumed to be equal:

$$\int_{k_{min}}^{k_{max}} [\Phi_{T_x}(k)]_{obs} dk = \int_{k_{min}}^{k_{max}} [\Phi_{T_x}(k)]_{theory} dk \quad (5)$$

152 An iterative procedure is then used to fit and calculate  $\chi$  and  $\varepsilon$ :

153 1. First we estimate  $\chi_T$  based on an initial guess of  $\varepsilon = 10^{-7}$  Wkg $^{-1}$  and compute  $k_b$  via eq. 3.

154 We set  $k_{max} = k_b/2$  or to a wavenumber equivalent to  $f_{max} = 7$  Hz [i.e.,  $k_{max} = 2\pi(f_{max})/u$ ],  
 155 whichever is smaller. In general  $f_{max}$  should be the highest value which is safely below the  
 156 sensor's roll-off. We chose  $f_{max} = 7$  Hz in this case based on inspection of the temperature  
 157 gradient spectra and historical measurements of these sensors (see appendix for more details).

158 2. We then use Eq. (4) to refine our estimate of  $\varepsilon$  and  $k_b$  and recompute  $\chi_T$  using Eqs. (1) and  
 159 (5).

160 3. This sequence is repeated and converges after two or three iterations.

161 Note that this procedure is equivalent to the explicit formulation of (Alford and Pinkel 2000),  
 162 except we use the Kraichnan theoretical form instead of the Batchelor spectrum for  $[\Phi_{T_x}(k)]_{theory}$ .  
 163 At wavenumbers below the spectral peak, there is little distinction between the Kraichnan and  
 164 Batchelor spectra, so this factor does not affect the computational bias.

### 165 b. CTD- $\chi$ pod Data Processing

166 We next review the basic outline for processing each CTD- $\chi$ pod profile. The moored  $\chi$ pod in-  
 167 strument (Moum and Nash 2009) has a pressure sensor, compass, and pitot-static tube. In contrast,

<sub>168</sub> the CTD- $\chi$ pod requires pressure measured by the CTD and has no independent speed measure-  
<sub>169</sub> ment other than  $dp/dt$  from the CTD.

<sub>170</sub> 1. The correct time-offset for the  $\chi$ pod clock is determined by aligning highpass-filtered  $dp/dt$   
<sub>171</sub> from the 24Hz CTD data to integrated vertical accelerations measured by the  $\chi$ pod.  $\chi$ pod  
<sub>172</sub> clock drift is small, typically on the order of 1 sec/week, but it is imperative to get records  
<sub>173</sub> aligned within < 0.5 s so that the correct value of  $u$  is used. In the case of the CTD- $\chi$ pod we  
<sub>174</sub> assume  $u$  is solely due to the vertical motion of the CTD cage, i.e.  $u = dp/dt$ .

<sub>175</sub> 2. Low-order polynomial calibration coefficients are determined to convert thermistor voltages  
<sub>176</sub> from  $\chi$ pod to ITS90 temperature (as measured by the CTD). Figure 4 shows an example of  
<sub>177</sub> the aligned and calibrated CTD- $\chi$ pod timeseries for one cast. Note the significant differences  
<sub>178</sub> in amount of variance associated with the two sensors during down and up casts. For the  
<sub>179</sub> upward-mounted sensor (T1), the downcast signal is largely associated with the CTD wake,  
<sub>180</sub> as is the upcast for the downward-mounted sensor (T2). Only the ‘clean’ portions of the cast  
<sub>181</sub> (e.g., the T1 upcast and the T2 downcast) are used in the  $\chi$ pod calculations.

<sub>182</sub> 3. Depth loops are identified and flagged in the 24Hz CTD data (Figure 5).  $\chi$ pod data during  
<sub>183</sub> these times are discarded since the signals are likely contaminated by the wake of the CTD.  
<sub>184</sub> We use a vertical velocity threshold of 0.3m/s and throw out data within 2m of the identified  
<sub>185</sub> loops. Even for profiles that are significantly affected by ship heaving, good segments of data  
<sub>186</sub> are obtained over a majority of the depths after removing contaminated data, allowing us to  
<sub>187</sub> compute values in nearly every 10m bin.

<sub>188</sub> 4. Buoyancy frequency  $N^2$  and temperature gradient  $dT/dz$  are computed from 1-m binned  
<sub>189</sub> CTD data, and averaged over a scale of 10m. The results are not very sensitive to the averag-  
<sub>190</sub> ing interval (see appendix for more details).

191        5. Half-overlapping 1 sec windows of data are used to estimate  $\chi$  following the methods de-  
192        scribed in Moum and Nash (2009), as outlined in the previous section.

193        *c. Example Spectra and Fits*

194        Examples of the observed (from FP07 thermistor on Chameleon) and fit spectra are shown in  
195        Figure 6, for two windows where a low and high dissipation rate was observed. The Chameleon  
196        spectra (magenta) shown is the theoretical Kraichnan spectra for the values of  $\chi$  and  $\varepsilon$  estimated  
197        using the shear-probe data. The  $\chi_{\text{pod}}$  fit is the estimate from applying the  $\chi_{\text{pod}}$  method to just  
198        the thermistor data for the same window. Note that at lower  $\varepsilon$ , a larger fraction of  $k_b$  is observed  
199        and the peak of the spectrum is almost resolved. At higher  $\varepsilon$ , less of the spectrum is resolved and  
200        the spectral peak is well above the maximum resolved wavenumber. Even so, the iterative  $\chi_{\text{pod}}$   
201        method gives an accurate estimate of  $\chi$ . The  $\chi_{\text{pod}}$  and Chameleon fits are performed over the  
202        same wavenumber range and thus match there. However, the higher-wavenumber portions of the  
203        fit spectra differ since the Chameleon fits use the observed  $k_b$  to determine the wavenumber extent.

204        **4. Results**

205        *a. Direct Test of  $\chi_{\text{pod}}$  Method*

206        We begin by utilizing the highly-resolved data from the freely-falling turbulence profiler,  
207        Chameleon (for which both  $\varepsilon$  and  $\chi$  are measured) to test the assumptions in our method of esti-  
208        mating  $\chi$ . We first apply the  $\chi_{\text{pod}}$  method to each Chameleon profile, using only the FP07 ther-  
209        mistor data. These results, which we refer to as  $\chi_{\chi}^{\text{cham}}$  and assume no independent knowledge of  
210         $\varepsilon$ , are then compared to  $\chi_{\varepsilon}^{\text{cham}}$ , computed by integrating the theoretical temperature gradient spec-  
211        trum where  $k_b$  is computed directly from shear-probe derived  $\varepsilon$ . Qualitatively,  $\chi_{\chi}^{\text{cham}}$  and  $\chi_{\varepsilon}^{\text{cham}}$   
212        show very similar depth and time patterns (Figure 7) and appear to agree in magnitude. A more

213 quantitative comparison (Figure 8), shows the two are well-correlated over five orders of magni-  
214 tude. The distribution of  $\log_{10}$  of the  $\chi$  ratios is approximately normal, with a mean of  $\mu = -0.1$   
215 and standard deviation of  $\sigma = 0.51$ . This indicates a low bias of  $\chi_{\chi}^{cham}$  relative to  $\chi_{\varepsilon}^{cham}$  of 20%  
216 and random variation of a factor of 3. The magnitude of the bias increases slightly at higher values  
217 of  $\varepsilon_{cham}$  (Table 1), reaching a low bias of approximately 40% for  $-6 < \log_{10}[\varepsilon_{cham}] < -5$ . The  
218 cause of this bias is unknown, but may be related to the spectrum shifting to higher wavenumbers  
219 at larger  $\varepsilon$ .

220 b. *CTDχpod - Chameleon Comparison*

221 Having demonstrated that the method works using Chameleon data, we now compare  $\chi_{\chi}^{ctd}$  from  
222 CTD-mounted  $\chi$ pods to  $\chi_{\varepsilon}^{cham}$ . In contrast to the Chameleon data, the CTD is more strongly  
223 coupled to the ship, and therefore subject to more vibration, heaving, and artificial turbulence  
224 created by the rosette. A total of 35 CTD- $\chi$ pod casts were performed, bracketed with Chameleon  
225 profiles immediately before and after. We first compare CTD- $\chi$ pod profiles to the mean of the  
226 two Chameleon profiles bracketing each cast, both averaged in 5m depth bins (Figure 9). The  
227 two are correlated, with considerable scatter. A histogram of the log of ratios is approximately  
228 normal and has a mean of  $-0.31$ , indicating a small negative bias. Since we expect significant  
229 natural variability in turbulence even between adjacent Chameleon profiles, we investigate further  
230 to determine if the observed  $\chi$ pod variability is of a similar magnitude or greater than expected.  
231 Scatter plots of before vs. after Chameleon profiles (not shown), typically separated by about  
232 an hour, show a similar level of scatter as the differences between methods, suggesting that the  
233 observed differences (Figure 9) can be explained by natural variability in turbulence. This is  
234 further demonstrated by histograms of the ratio of  $\chi$  from adjacent casts (Figure 10) which show  
235 that the variability between CTD  $\chi$ pod and Chameleon casts is similar to the natural variability

236 between before/after Chameleon profiles. Profiles from all CTD-Chameleon pairs averaged in time  
237 and 40m depth bins (Figure 11) overlap within 95% confidence limits at all depths where there  
238 exists good data for both. Averages of subsets of these profiles that were clustered in position/time  
239 (not shown) also agree well. We conclude that the variability between CTD $\chi$ pod and Chameleon  
240 profiles is indistinguishable from natural variability in turbulence levels.

241 **5. Discussion**

242 We have shown that  $\chi$  can be accurately estimated from  $\chi$ pods attached to CTD rosettes. The  
243 method also estimates  $K_T$  and  $\varepsilon$ , but we have left discussion of these for a future paper since they  
244 involve more assumptions and uncertainties. One major assumption is the mixing efficiency  $\Gamma$ . A  
245 value of 0.2 is commonly assumed, but evidence suggests this may vary significantly. Moum and  
246 Nash (2009) found a bias in  $\chi$  of up to 1.6 for  $\Gamma$  values ranging from 0.1 to 0.35. Another major  
247 assumption in the  $\chi$ pod method is that  $K_T = K_P$  (Moum 1996).

248 The goal of CTD- $\chi$ pods is to expand the number and spatial coverage of ocean mixing obser-  
249 vations. The census of Waterhouse et al. (2014) found less than 20 locations where full-depth  
250 microstructure profiles were taken (see their figure 1c), all of which had less than 100 profiles. We  
251 have already deployed CTD  $\chi$ pods during several process experiments and on several GO-SHIP  
252 repeat-hydrography cruises, obtaining more than 1700 full-depth profiles of  $\chi$  over a wide range  
253 of locations. We plan to continue regular deployment on GO-SHIP and similar cruises, adding  
254  $\chi$  to the suite of variables regularly measured. The expanding database of mixing measurements  
255 from CTD- $\chi$ pods will also enable testing of other commonly-used or new mixing parameteriza-  
256 tions. This has the potential to be transformative for the field, allowing the community to develop  
257 and test global turbulence parameterizations, use estimates of turbulence along with the CLIVAR  
258 repeat hydrography data for inverse models and water mass modification calculations, identify

259 hotspots of turbulence to target with future process experiments, and compare with in-situ chemi-  
260 cal and biological measurements made routinely on repeat hydrography cruises.

261 **6. Conclusions**

- 262 • The  $\chi$ pod method for estimating  $\chi$  was directly applied to temperature gradients measured  
263 by the Chameleon microstructure profiler on > 2700 profiles during the EQ14 cruise. The  
264 estimated  $\chi_\chi$  agrees well with  $\chi_\varepsilon$  calculated using  $\varepsilon$  from shear probes over a wide range of  
265 magnitudes (Figure 8) with little or no bias, demonstrating that the method works.
- 266 • CTD- $\chi$ pod profiles were also compared to nearby Chameleon profiles during the cruise. Vari-  
267 ability between CTD- $\chi$ pod and Chameleon estimates of  $\chi$  is indistinguishable from natural  
268 variability between Chameleon profiles. Time-averaged profiles of  $\chi$  from both platforms  
269 agree within 95% confidence limits, and no significant bias was detected between the esti-  
270 mates of  $\chi$ .
- 271 • We conclude that estimates of  $\chi$  made from the CTD- $\chi$ pod platform are robust and reliable.

272 *Acknowledgments.* The EQ14 experiment was funded by budget (NSF?) 1256620. We thank the  
273 Captain and crew of R/V Oceanus. Pavan Vutukur, Craig Van Appledorn, Mike Neeley-Brown  
274 made the sensors. Aurelie Moulin, Ryan Holmes, Sally Warner and Anna Savage helped to collect  
275 the data.

276 APPENDIX A

277 **Sensitivity Analysis**

278 **A1. Flowspeed Past Sensor**

279 To quantify the potential error in the CTD- $\chi$ pod calculations from ignoring horizontal velocities  
280 and assuming the flow speed is equal to the vertical speed of the CTD rosette, we repeated the  
281 calculations with constant offsets added to the flowspeed. Note that since the total magnitude of  
282 velocity is used,  $dp/dt$  is a minimum estimate of the true speed. Adding 0.1(1)m/s results in a  
283 mean percent error of -14(-58) percent (Figure 12), small compared the large natural variability in  
284 turbulence and uncertainty in our measurements. Note that increasing the velocity tends to result  
285 in smaller values of  $\chi$ , since it shifts the spectrum to lower wavenumbers.

286 We also looked for any systematic biases associated with flowpseed. We found that  $\chi$  was biased  
287 high for very small speeds ( $u < 25\text{cm/s}$ ). This could be associated with contamination by CTD  
288 wake or entrained water when the CTD slows. These values were discarded for our analysis.

289 **APPENDIX B**

290 **Test of MLE fitting method**

291 We also tested the spectrum fitting method of Ruddick et al. (2000) and compared to our  $\chi$ pod  
292 method. The MLE method works well and gives similar results to our method at true  $\epsilon$  values  
293 less than about  $10^{-9}$ , but severely underestimates  $\chi$  at larger values of epsilon, where only a small  
294 fraction of the spectrum is resolved (Figure 13). At lower profiling speeds we would expect the  
295 MLE method to work better, as more of the spectrum will be resolved for a given value of  $\epsilon$ .

296 **APPENDIX C**

297 **Thermistor Frequency Response**

298 Prior to 2009, the transfer function for each FP07 thermistor was measured by profiling adjacent  
299 to a thermocouple in Yaquina Bay, OR. However, measuring the transfer function for each indi-  
300 vidual thermistor proved too expensive and time-consuming, and since that time a generic transfer  
301 function has been used. Figure 14 shows the measured transfer functions for 2008. The majority  
302 of the transfer functions are similar for frequencies up to about 10 Hz, and begin to significantly  
303 differ above that. To estimate the potential error in not using a transfer function, we calculated the  
304 % of spectral variance captured for each of the measured functions. For frequencies up to 7Hz,  
305 more than 95% is captured for 88% of the measured functions. If frequencies up to 15hz are used,  
306 more than 95 % variance is captured only 67% of the time. Using only frequencies up to 7Hz  
307 (where the transfer function is equal to or very close to unity) avoids the issue of the unknown  
308 transfer functions.

## 309 References

- 310 Alford, M., and R. Pinkel, 2000: Patterns of turbulent and double diffusive phenomena: Observa-  
311 tions from a rapid profiling conductivity probe. *J. Phys. Oceanogr.*, **30**, 833–854.
- 312 Batchelor, G. K., 1959: Small-scale variation of convected quantitites like temperature in turbulent  
313 fluid. *J. Fluid Mech.*, **5**, 113–139.
- 314 Dillon, T. M., 1982: Vertical overturns: A comparison of Thorpe and Ozmidov length scales. *J.*  
315 *Geophys. Res.*, **87**, 9601–9613.
- 316 Galbraith, P. S., and D. E. Kelley, 1996: Identifying overturns in CTD profiles. *J. Atmos. Ocean.*  
317 *Tech.*, **13**, 688–702.
- 318 Gregg, M., 1989: Scaling turbulent dissipation in the thermocline. *J. Geophys. Res.*, **94 (C7)**,  
319 9686–9698.

- 320 Holmes, R., J. Moum, and L. Thomas, 2016: Evidence for seafloor-intensified mixing by surface-  
321 generated equatorial waves. *Geophysical Research Letters*, **43** (3), 1202–1210.
- 322 Kunze, E., E. Firing, J. Hummon, T. K. Chereskin, and A. Thurnherr, 2006: Global abyssal mixing  
323 inferred from lowered ADCP shear and CTD strain profiles. *Journal of Physical Oceanography*,  
324 **36** (8), 1553–1576.
- 325 Mater, B. D., S. K. Venayagamoorthy, L. S. Laurent, and J. N. Moum, 2015: Biases in Thorpe scale  
326 estimates of turbulence dissipation Part I: Assessments from large-scale overturns in oceanogra-  
327 phic data. *J. Phys. Oceanogr.*, **45** (2015), 2497–2521.
- 328 Melet, A., R. Hallberg, S. Legg, and K. L. Polzin, 2013: Sensitivity of the ocean state to the  
329 vertical distribution of internal-tide-driven mixing. *J. Phys. Oceanogr.*, **43** (3), 602–615, doi:  
330 <http://dx.doi.org/10.1175/JPO-D-12-055.1>.
- 331 Moum, J., M. Gregg, R. Lien, and M. Carr, 1995: Comparison of turbulence kinetic energy dis-  
332 sipation rate estimates from two ocean microstructure profilers. *Journal of Atmospheric and*  
333 *Oceanic Technology*, **12** (2), 346–366.
- 334 Moum, J., and J. Nash, 2009: Mixing measurements on an equatorial ocean mooring. *J. Atmos.*  
335 *Ocean. Tech.*, **26**, 317–336.
- 336 Moum, J. N., 1996: Efficiency of mixing in the main thermocline. *Journal of Geophysical Re-*  
337 *search*, **101** (C5), 12 057–12 069.
- 338 Moum, J. N., 2015: Ocean speed and turbulence measurements using pitot-static tubes on moor-  
339 ings. *Journal of Atmospheric and Oceanic Technology*, (2015).
- 340 Munk, W., and C. Wunsch, 1998: Abyssal recipes II: energetics of tidal and wind mixing. *Deep-*  
341 *Sea Res. Part I*, **45**, 1977–2010.

- 342 Munk, W. H., 1966: Abyssal recipes. *Deep-Sea Res.*, **13**, 707–730.
- 343 Osborn, T. R., 1980: Estimates of the local rate of vertical diffusion from dissipation measure-  
344 ments. *J. Phys. Oceanogr.*, **10**, 83–89.
- 345 Osborn, T. R., and C. S. Cox, 1972: Oceanic fine structure. *Geophys. Fluid Dyn.*, **3**, 321–345.
- 346 Polzin, K. L., A. C. Naveira Garabato, T. N. Huussen, B. M. Sloyan, and S. Waterman,  
347 2014: Finescale parameterizations of turbulent dissipation. *Journal of Geophysical Research:  
348 Oceans*, **119** (2), 1383–1419, doi:10.1002/2013JC008979, URL <http://dx.doi.org/10.1002/2013JC008979>.
- 349 Ruddick, B., A. Anis, and K. Thompson, 2000: Maximum likelihood spectral fitting: The Batch-  
350 elor spectrum. *J. Atmos. Ocean. Tech.*, **17**, 1541–1555.
- 351 Scotti, A., 2015: Biases in Thorpe scale estimates of turbulence dissipation Part II: Energetics  
352 arguments and turbulence simulations. *J. Phys. Oceanogr.*, **45** (2015), 2522–2543.
- 353 Thorpe, S., 1977: Turbulence and mixing in a Scottish Loch. *Philos. Trans. R. Soc. London Ser.  
354 A*, **286**, 125–181.
- 355 Waterhouse, A. F., and Coauthors, 2014: Global patterns of diapycnal mixing from measurements  
356 of the turbulent dissipation rate. *J. Phys. Oceanogr.*, **44** (7), 1854–1872.
- 357 Waterman, S., A. C. N. Garabato, and K. L. Polzin, 2013: Internal waves and turbulence in the  
358 antarctic circumpolar current. *Journal of Physical Oceanography*, **43** (2), 259–282.
- 359 Whalen, C. B., J. A. MacKinnon, L. D. Talley, and A. F. Waterhouse, 2015: Estimating the  
360 mean diapycnal mixing using a finescale strain parameterization. *Journal of Physical Oceanog-  
361 raphy*, **45** (4), 1174–1188, doi:10.1175/JPO-D-14-0167.1, URL <http://dx.doi.org/10.1175/JPO-D-14-0167.1>.

<sup>364</sup> Whalen, C. B., L. D. Talley, and J. A. MacKinnon, 2012: Spatial and temporal variabil-  
<sup>365</sup> ity of global ocean mixing inferred from argo profiles. *Geophys. Res. Lett.*, **39** (L18612),  
<sup>366</sup> doi:10.1029/2012GL053196.

<sup>367</sup> **LIST OF TABLES**

<sup>368</sup> **Table 1.** Biases and stand. dev. of ratios of  $\log_{10}[\chi_\chi/\chi_\varepsilon]$  for different ranges of  $\varepsilon_{cham}$ . . . . . 21

TABLE 1. Biases and stand. dev. of ratios of  $\log_{10}[\chi_\chi/\chi_\varepsilon]$  for different ranges of  $\varepsilon_{cham}$ .

$\varepsilon_{cham}$ range	bias	sd
$-9 < \varepsilon < -8$	-0.04	0.47
$-8 < \varepsilon < -7$	-0.15	0.51
$-7 < \varepsilon < -6$	-0.18	0.54
$-6 < \varepsilon < -5$	-0.2	0.55

## 369 LIST OF FIGURES

370	<b>Fig. 1.</b> Top: Theoretical (Nasmyth) wavenumber spectra for velocity shear, for two different values 371 of $\varepsilon$ . Lower: Theoretical (Kraichnan) wavenumber spectra for temperature gradient, for two 372 different values of $\varepsilon$ and $\chi$ . Note the amplitudes of temperature gradient spectra depend on 373 both $\varepsilon$ and $\chi$ , while the shear spectra depend only on $\varepsilon$ . Diamonds indicate the Batchelor 374 wavenumber for each, which depends only on $\varepsilon$ . Vertical dashed lines indicate range of 375 wavenumbers used for $\chi$ pod fit assuming $u = 1\text{m/s}$ . . . . .	24
376	<b>Fig. 2.</b> Photo of CTD rosette during EQ14 with $\chi$ pods attached. . . . .	25
377	<b>Fig. 3.</b> Ratio of the maximum observed wavenumber $k_{max} = f_{max}/u$ to the Batchelor wavenumber 378 $k_b$ for different values of $\varepsilon$ , assuming a $f_{max} = 7\text{Hz}$ . Each line is for a different flowspeed. . . . .	26
379	<b>Fig. 4.</b> Example timeseries from one CTD cast during EQ14. a) CTD pressure. b) Fallspeed of 380 CTD ( $dp/dt$ ) .c) Vertical and horizontal accelerations measured by $\chi$ pod. d) Temperature 381 from CTD and (calibrated) $\chi$ pod sensors. T2 is offset slightly for visualization. e) Temper- 382 ature derivative $dT/dt$ measured by the upward-looking $\chi$ pod sensor T1. f) Temperature 383 derivative $dT/dt$ measured by the downward-looking $\chi$ pod sensor T2. . . . .	27
384	<b>Fig. 5.</b> Portion of a CTD cast showing depth vs time (top) during an upcast, with data flagged as 385 loops in red. Lower panel shows corresponding $\chi$ pod timeseries of $dT/dt$ for that time with 386 discarded loop data in red. Note that variance tends to be larger during depth loops due to 387 entrained water and CTD-induced turbulence. . . . .	28
388	<b>Fig. 6.</b> Two example temperature gradient spectra from an EQ14 Chameleon profile, for high (top) 389 and low (bottom) values of $\varepsilon$ . Solid black lines with circles show the observed temperature- 390 gradient spectra from the thermistor on Chameleon. Dashed black line shows the fitted 391 theoretical Kraichnan spectra estimated by applying the $\chi$ pod method to the thermistor data 392 only. Magenta line is Kraichnan spectra for Chameleon $\chi$ and $\varepsilon$ measured at the same depth, 393 using the shear probe data as well. Vertical dashed blue(red) lines indicate the minimum 394 (maximum) wavenumber used in the $\chi$ pod calculation. The Batchelor wavenumber $k_b$ is 395 also indicated by the vertical magenta line. . . . .	29
396	<b>Fig. 7.</b> Depth-time plots of $\log_{10}\chi$ from both methods for EQ14 data. Top: $\chi$ pod method using 397 only FP07 data from Chameleon. Black diamonds indicate casts used for comparison with 398 CTD- $\chi$ pod profiles. Bottom: Chameleon measurements using FP07 and shear probe data. . . . .	30
399	<b>Fig. 8.</b> Top: 2D histogram of $\log_{10}(\chi)$ from Chameleon (x-axis) and $\chi$ pod method (y-axes). Values 400 from each profile were averaged in the same 5m depth bins. Bottom: Normalized histogram 401 of $\log_{10}[\chi_{\chi}^{cham}/\chi_{\varepsilon}^{cham}]$ . Vertical dashed line indicates the mean of the the distribution. . . . .	31
402	<b>Fig. 9.</b> Left: Scatter plot of $\chi$ from CTD- $\chi$ pod profiles versus the mean of bracketing Chameleon 403 profiles. Black dashed line shows 1:1, red are $\pm 10\chi$ . Right: Normalized histogram of the 404 log of ratios. . . . .	32
405	<b>Fig. 10.</b> Histogram of $\log_{10}$ of the ratio of $\chi$ for nearby casts. The first set is for the before ( $\chi_{\varepsilon 1}^{cham}$ ) 406 and after ( $\chi_{\varepsilon 2}^{cham}$ ) Chameleon profiles. The 2nd is CTD- $\chi$ pod profiles ( $\chi_{\chi}^{ctd}$ ) versus the 407 before( $\chi_{\varepsilon 1}^{cham}$ ) profiles. The last is CTD- $\chi$ pod profiles ( $\chi_{\chi}^{ctd}$ ) versus the after( $\chi_{\varepsilon 2}^{cham}$ ) pro- 408 files. Dashed lines show the medians of each set. Note that bias is small/zero, and the 409 variability (spread) between CTD/cham is similar to the natural variability between cham 410 profiles. . . . .	33

411	<b>Fig. 11.</b> Time mean of $\chi$ for all CTD- $\chi$ pod - Chameleon cast pairs, with 95% bootstrap confidence	34
412	intervals. . . . .	
413	<b>Fig. 12.</b> Histogram of % error for $\chi$ computed with constant added to fallspeed, in order to examine	35
414	sensitivity to fallspeed. Vertical lines indicate the mean of each distribution. . . . .	
415	<b>Fig. 13.</b> Left: 2D histograms of $\chi$ computed using the iterative $\chi$ pod method (top) and the MLE fit	36
416	(bottom) versus $\chi$ computed from Chameleon. Note that the MLE method underestimates	
417	$\chi$ at larger magnitudes. Right: Histograms of the log of ratios for different ranges of $\varepsilon$ . The	
418	mean of each distribution is given above. . . . .	
419	<b>Fig. 14.</b> Measured FP07 thermistor transfer functions from historical database. Vertical dashed lines	37
420	show the frequency range used in $\chi$ pod method. Dashed blue line is a generic transfer	
421	function found to best match measured functions. . . . .	

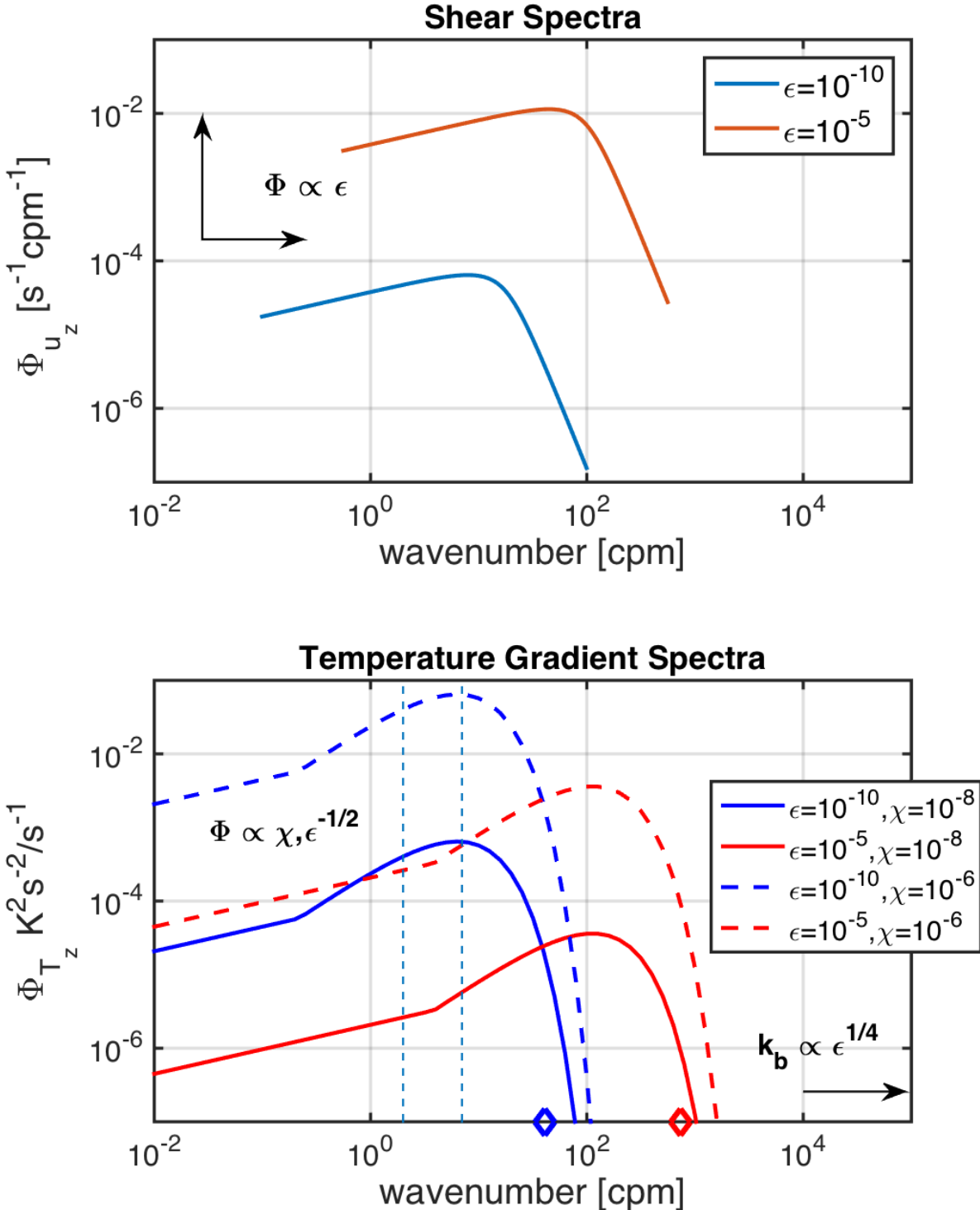


FIG. 1. Top: Theoretical (Nasmyth) wavenumber spectra for velocity shear, for two different values of  $\epsilon$ . Lower: Theoretical (Kraichnan) wavenumber spectra for temperature gradient, for two different values of  $\epsilon$  and  $\chi$ . Note the amplitudes of temperature gradient spectra depend on both  $\epsilon$  and  $\chi$ , while the shear spectra depend only on  $\epsilon$ . Diamonds indicate the Batchelor wavenumber for each, which depends only on  $\epsilon$ . Vertical dashed lines indicate range of wavenumbers used for  $\chi$  pod fit assuming  $u = 1\text{m/s}$ .<sup>24</sup>

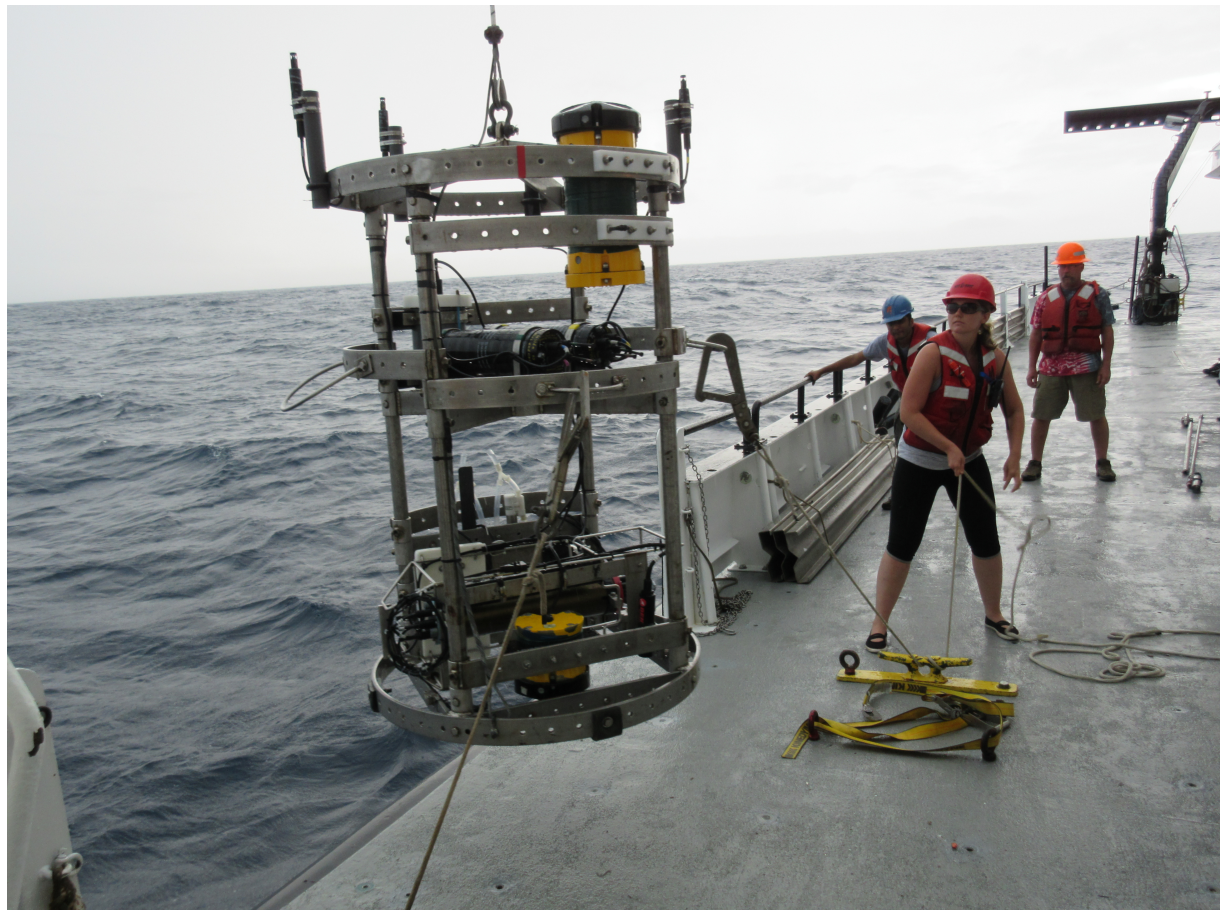
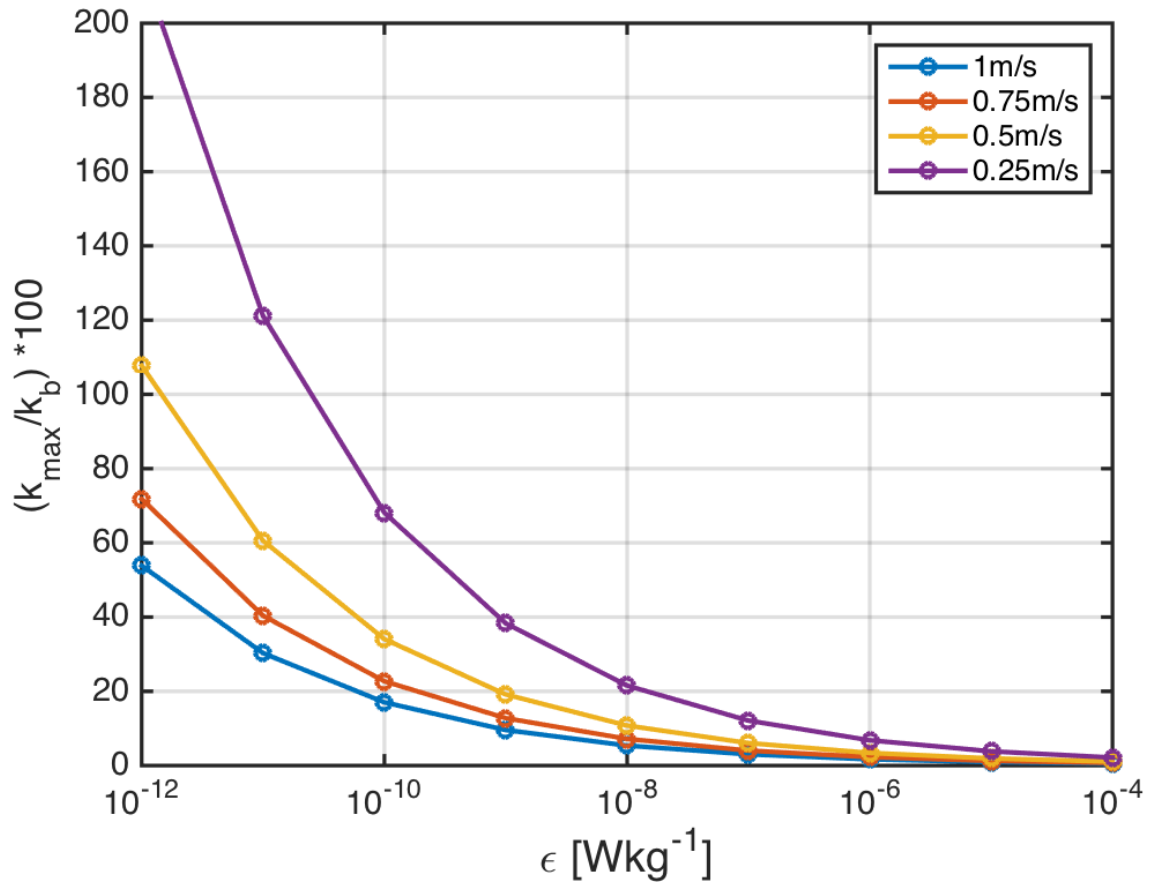
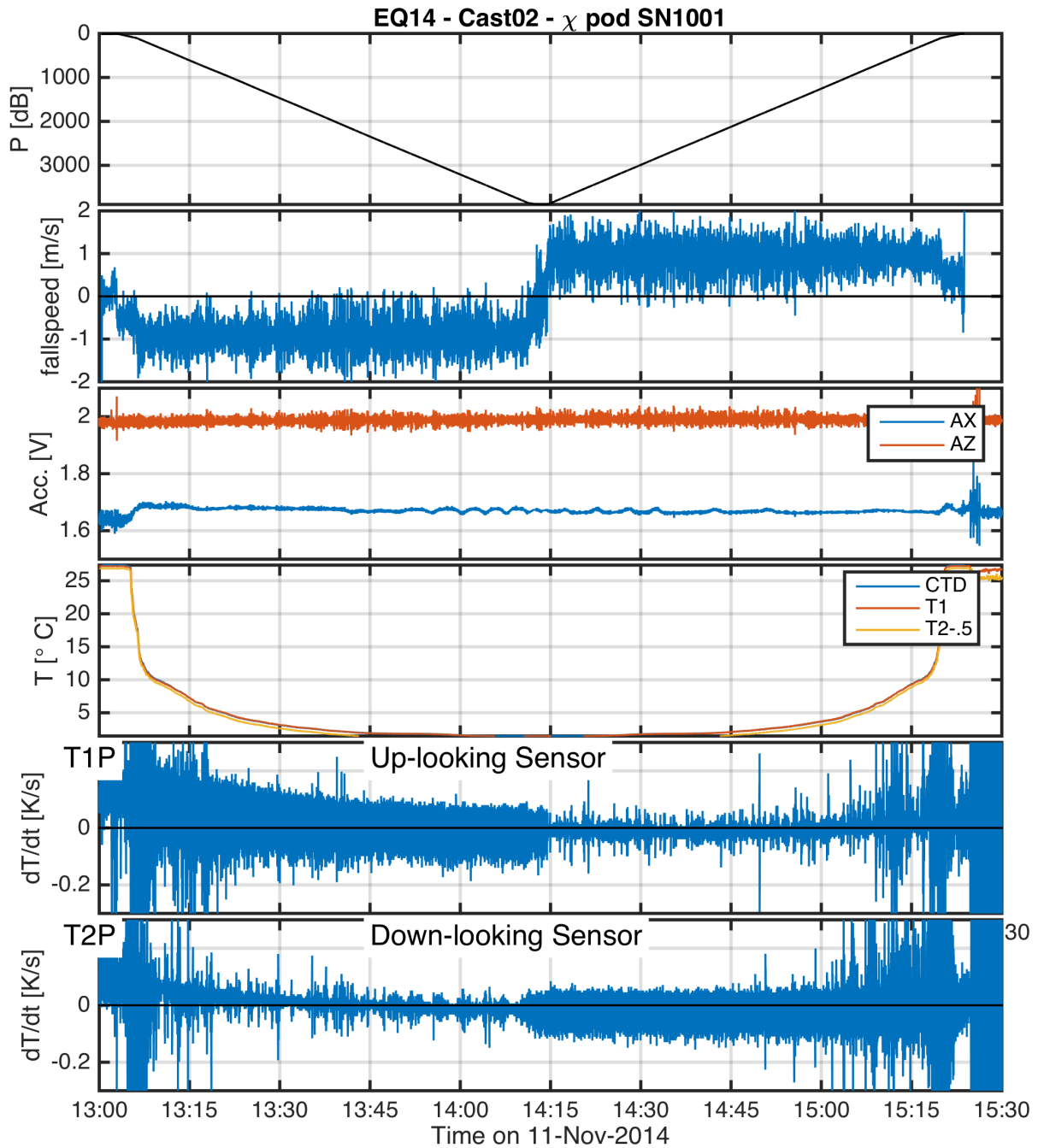


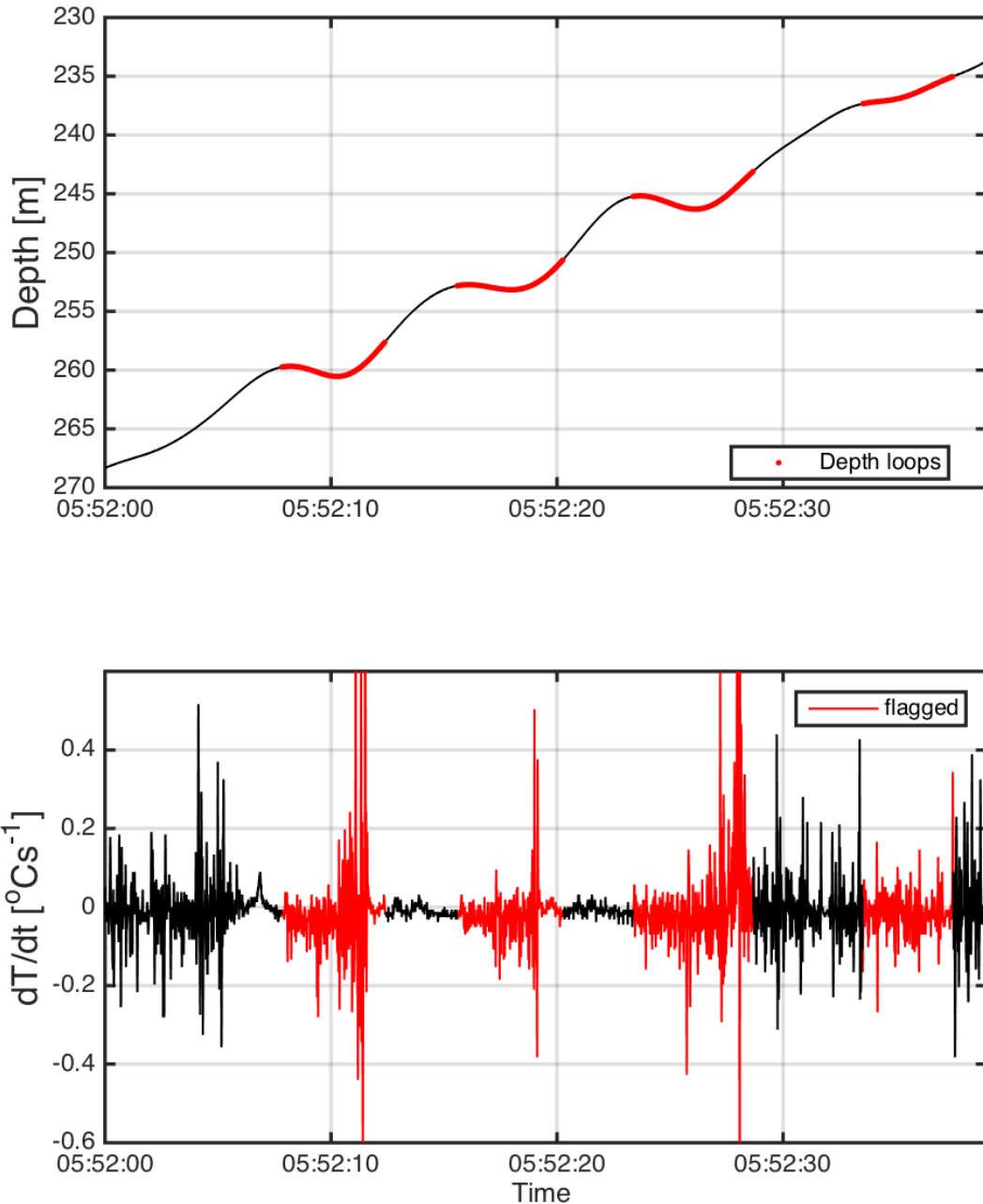
FIG. 2. Photo of CTD rosette during EQ14 with  $\chi$ pods attached.



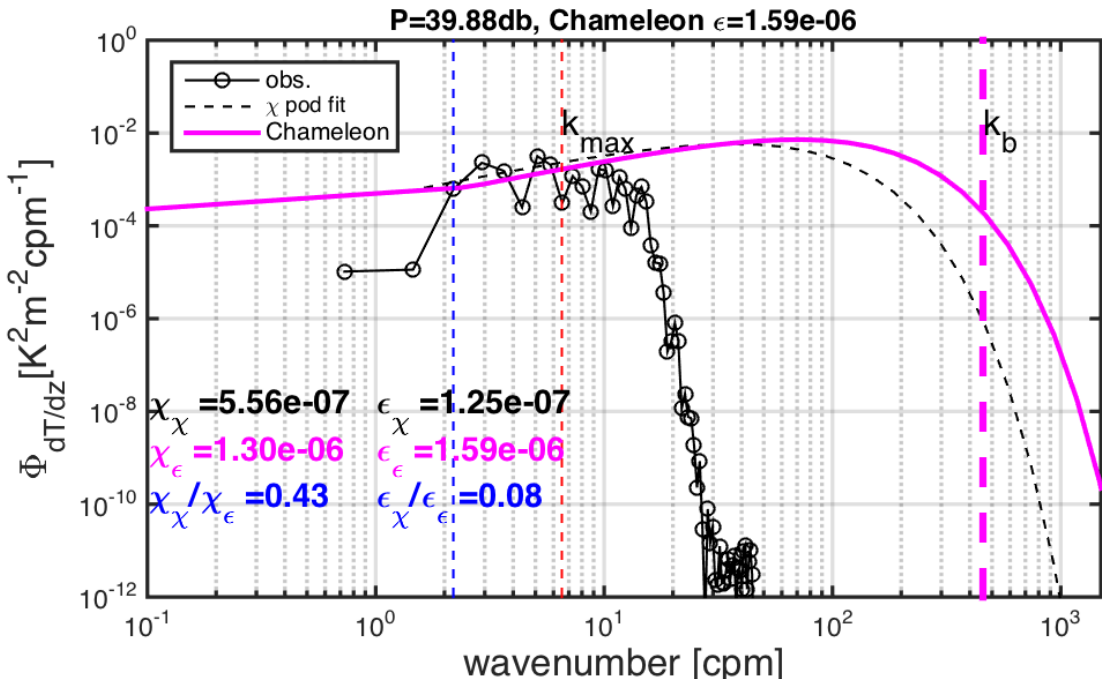
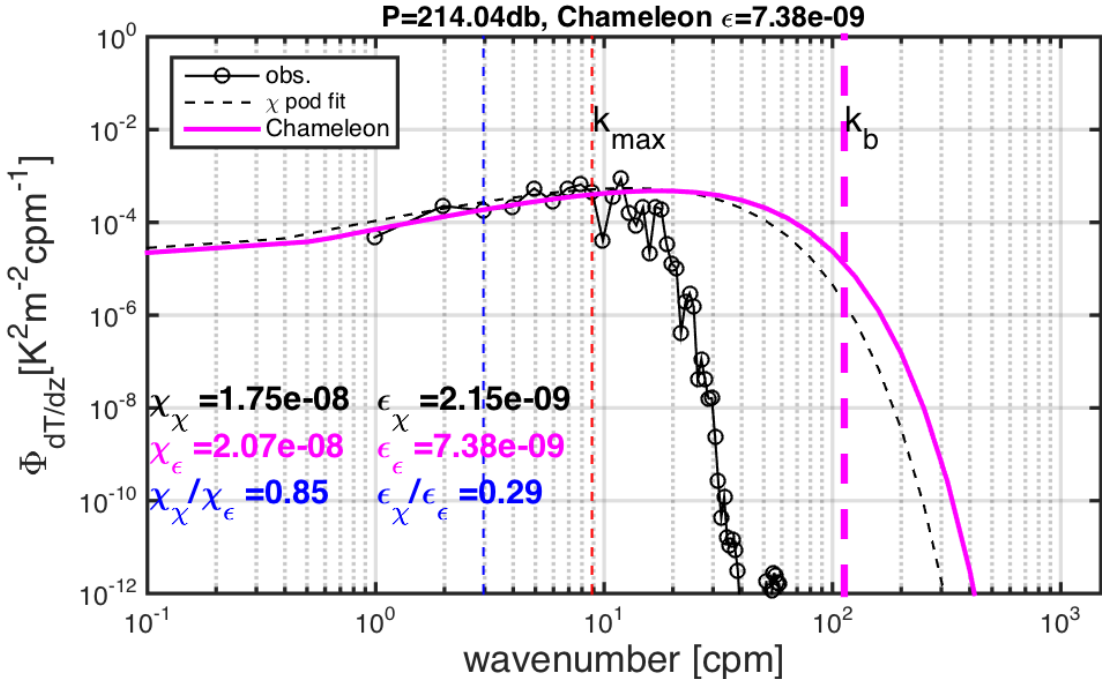
427 FIG. 3. Ratio of the maximum observed wavenumber  $k_{\max} = f_{\max}/u$  to the Bachelor wavenumber  $k_b$  for  
 428 different values of  $\epsilon$ , assuming a  $f_{\max} = 7\text{Hz}$ . Each line is for a different flowspeed.



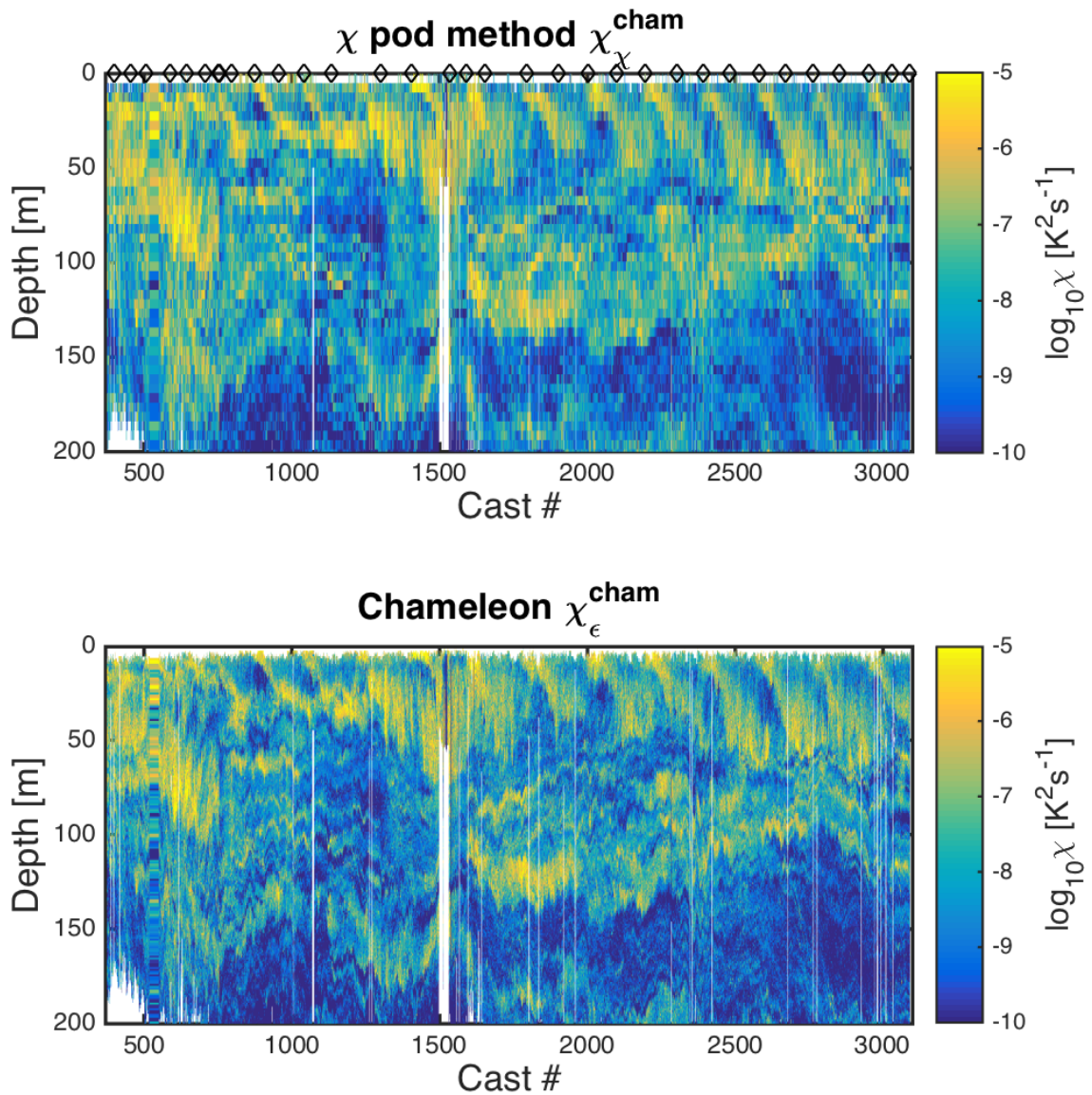
429 FIG. 4. Example timeseries from one CTD cast during EQ14. a) CTD pressure. b) Fallspeed of CTD ( $dp/dt$ )  
 430 .c) Vertical and horizontal accelerations measured by  $\chi$ pod. d) Temperature from CTD and (calibrated)  $\chi$ pod  
 431 sensors. T2 is offset slightly for visualization. e) Temperature derivative  $dT/dt$  measured by the upward-looking  
 432  $\chi$ pod sensor T1. f) Temperature derivative  $dT/dt$  measured by the downward-looking  $\chi$ pod sensor T2.



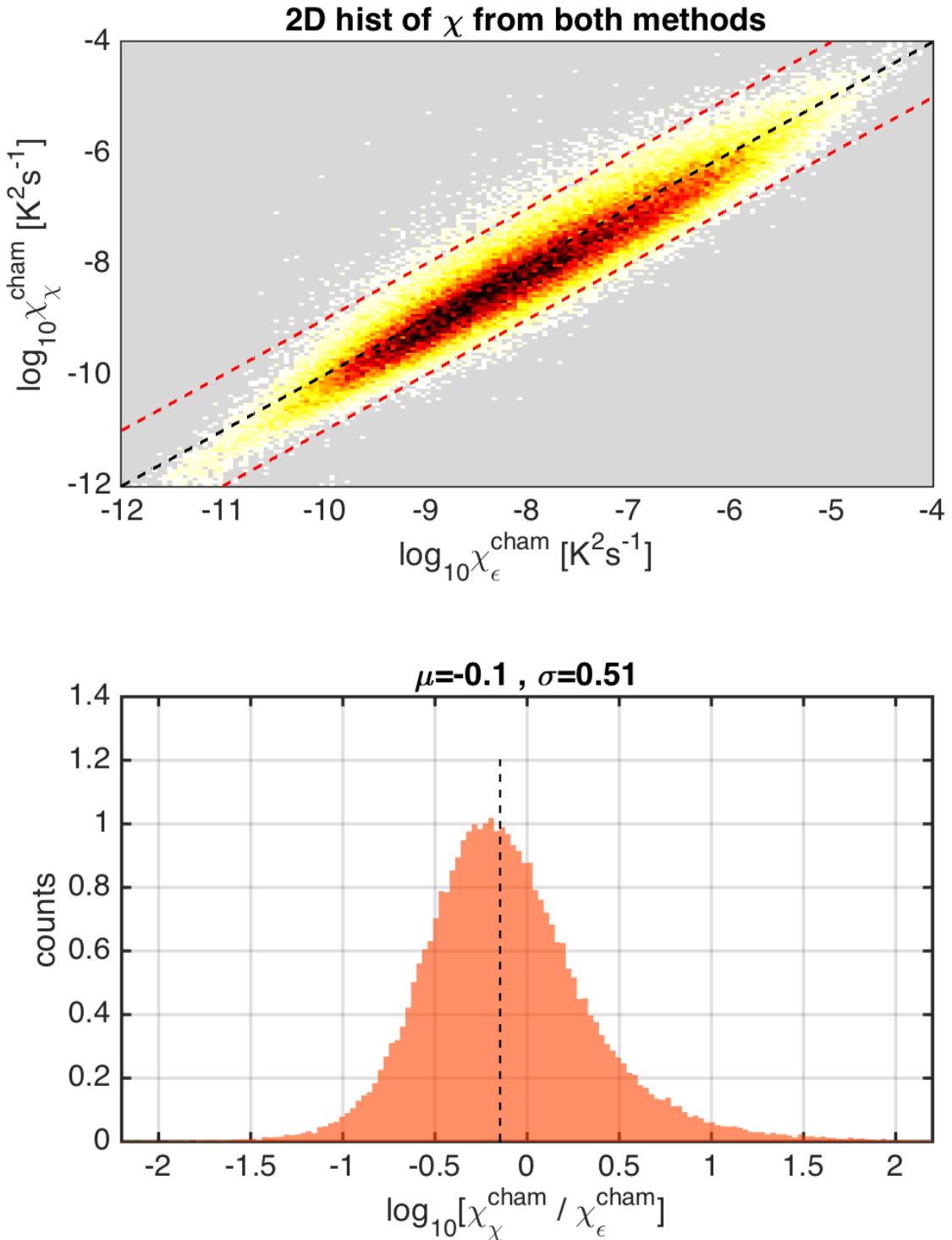
433 FIG. 5. Portion of a CTD cast showing depth vs time (top) during an upcast, with data flagged as loops in red.  
 434 Lower panel shows corresponding  $\chi$ pod timeseries of  $dT/dt$  for that time with discarded loop data in red. Note  
 435 that variance tends to be larger during depth loops due to entrained water and CTD-induced turbulence.



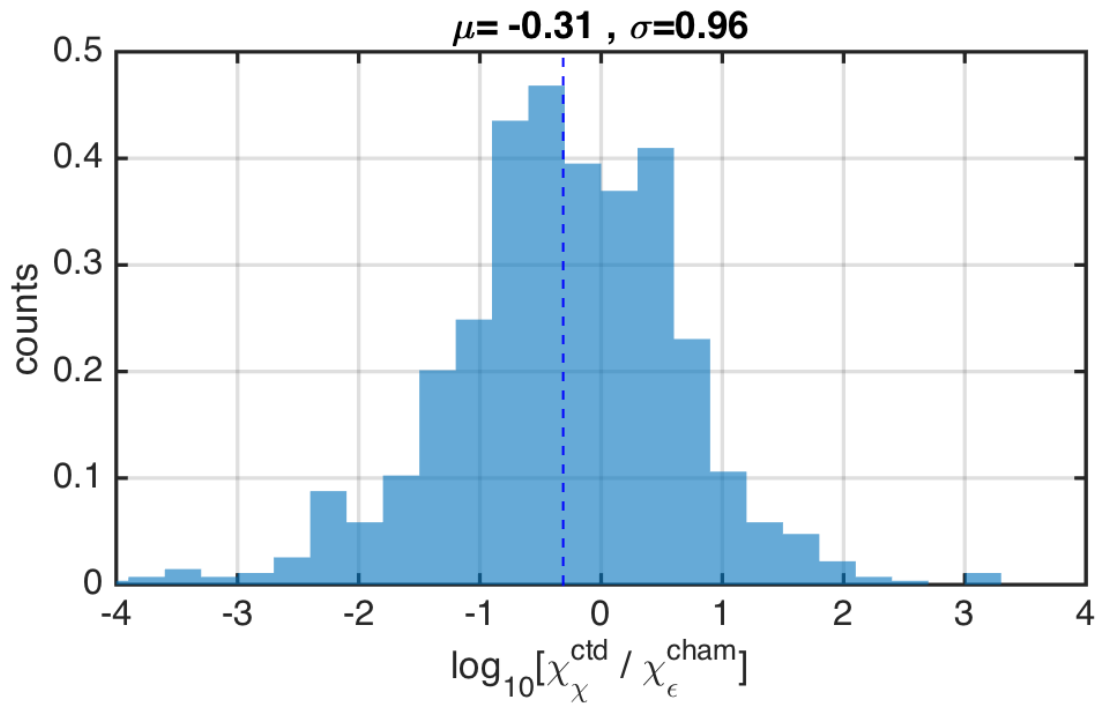
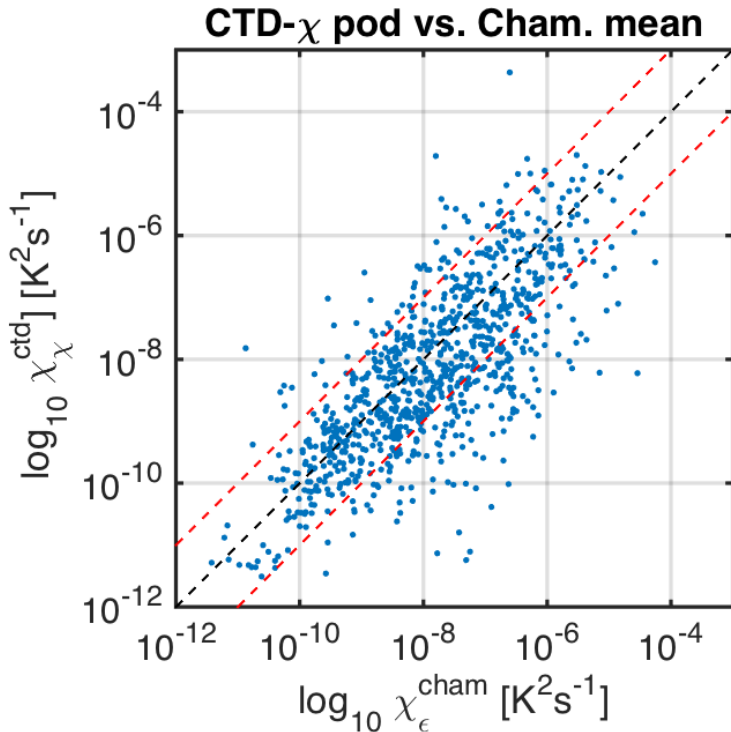
436 FIG. 6. Two example temperature gradient spectra from an EQ14 Chameleon profile, for high (top)  
437 and low (bottom) values of  $\epsilon$ . Solid black lines with circles show the observed temperature-gradient spectra from  
438 the thermistor on Chameleon. Dashed black line shows the fitted theoretical Kraichnan spectra estimated by  
439 applying the  $\chi$ pod method to the thermistor data only. Magenta line is Kraichnan spectra for Chameleon  $\chi$   
440 and  $\epsilon$  measured at the same depth, using the shear probe data as well. Vertical dashed blue(red) lines indicate  
441 the minimum (maximum) wavenumber used in the  $\chi$ pod calculation. The Batchelor wavenumber  $k_b$  is also



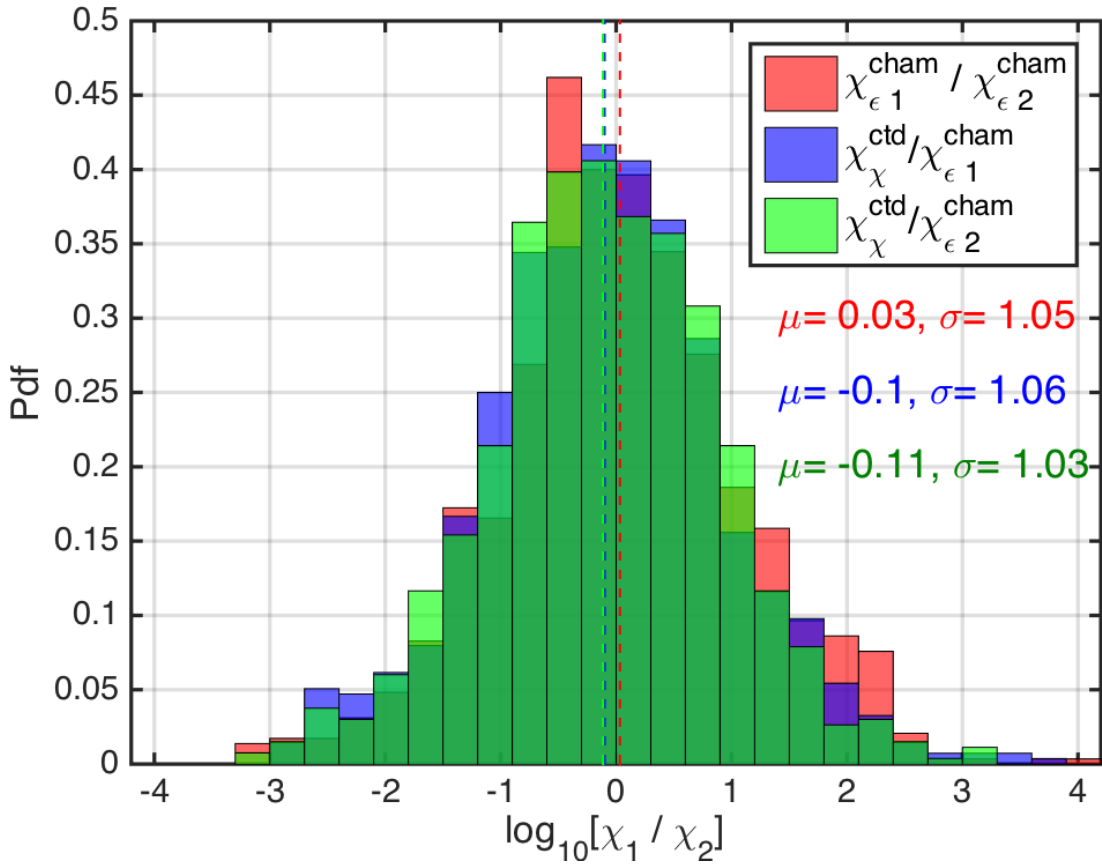
<sup>443</sup> FIG. 7. Depth-time plots of  $\log_{10}\chi$  from both methods for EQ14 data. Top:  $\chi$ pod method using only FP07  
<sup>444</sup> data from Chameleon. Black diamonds indicate casts used for comparison with CTD- $\chi$ pod profiles. Bottom:  
<sup>445</sup> Chameleon measurements using FP07 and shear probe data.



<sup>446</sup> FIG. 8. Top: 2D histogram of  $\log_{10}(\chi)$  from Chameleon (x-axis) and  $\chi_{\text{pod}}$  method (y-axes). Values from  
<sup>447</sup> each profile were averaged in the same 5m depth bins. Bottom: Normalized histogram of  $\log_{10}[\chi_{\chi}^{\text{cham}} / \chi_{\epsilon}^{\text{cham}}]$ .  
<sup>448</sup> Vertical dashed line indicates the mean of the the distribution.



449 FIG. 9. Left: Scatter plot of  $\chi$  from CTD- $\chi$ pod profiles versus the mean of bracketing Chameleon profiles.  
 450 Black dashed line shows 1:1, red are  $\pm 10$ . Right: Normalized histogram of the log of ratios.



451 FIG. 10. Histogram of  $\log_{10}$  of the ratio of  $\chi$  for nearby casts. The first set is for the before ( $\chi_{\epsilon 1}^{cham}$ ) and after  
 452 ( $\chi_{\epsilon 2}^{cham}$ ) Chameleon profiles. The 2nd is CTD- $\chi$ pod profiles ( $\chi_{\chi}^{ctd}$ ) versus the before( $\chi_{\epsilon 1}^{cham}$ ) profiles. The last is  
 453 CTD- $\chi$ pod profiles ( $\chi_{\chi}^{ctd}$ ) versus the after( $\chi_{\epsilon 2}^{cham}$ ) profiles. Dashed lines show the medians of each set. Note that  
 454 bias is small/zero, and the variability (spread) between CTD/cham is similar to the natural variability between  
 455 cham profiles.

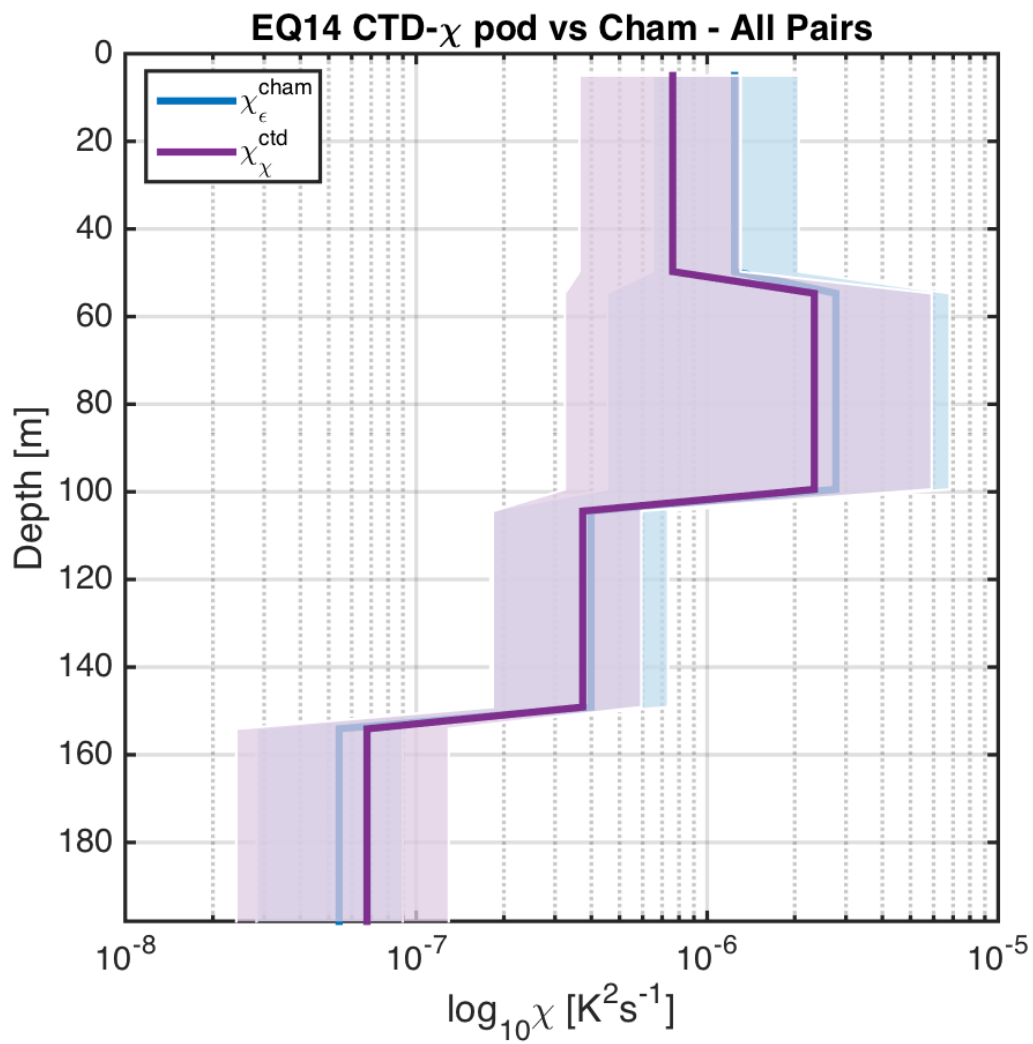
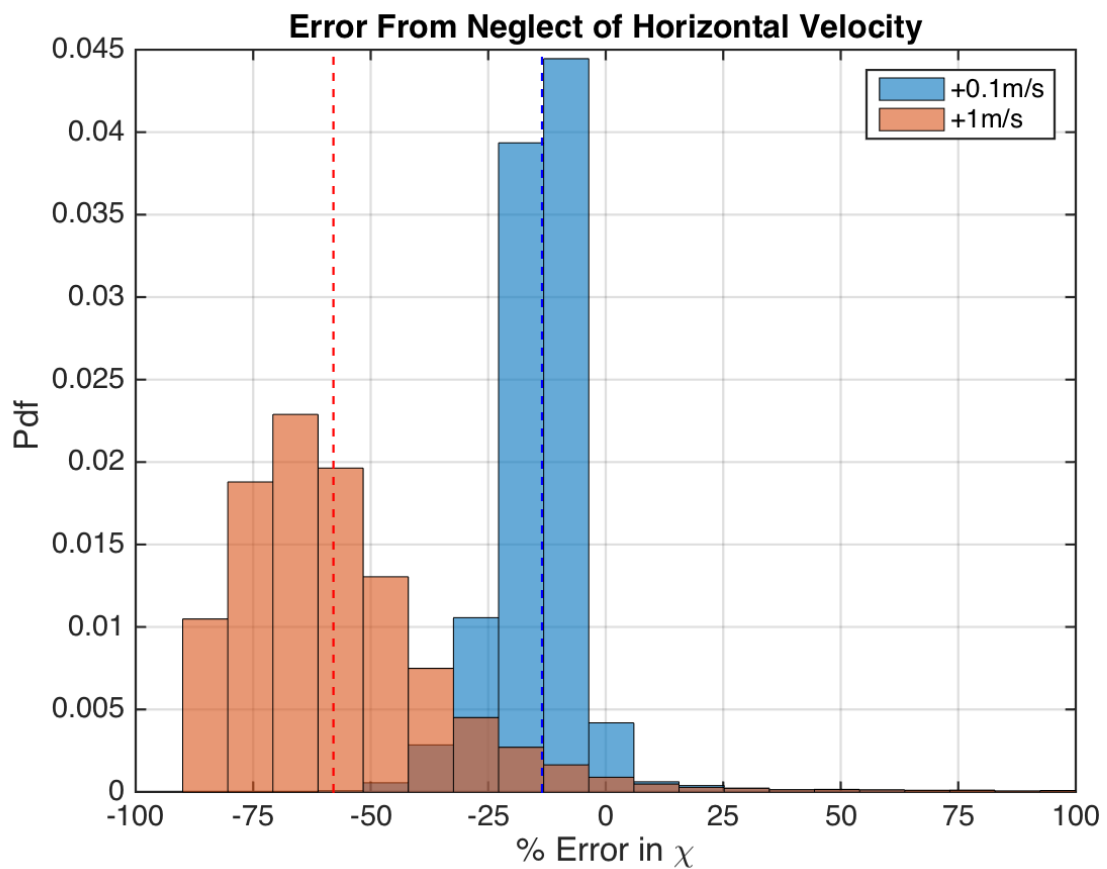
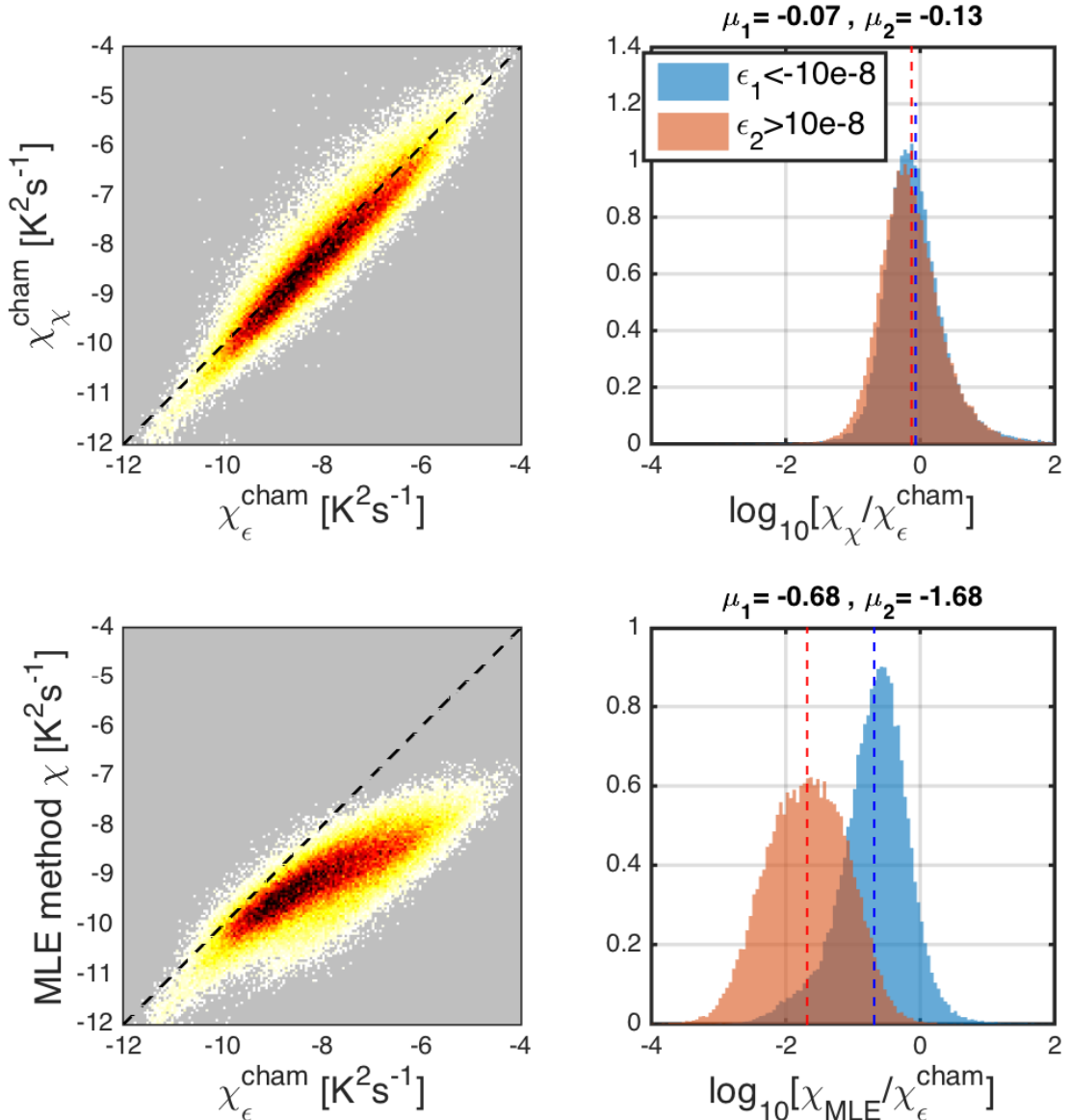


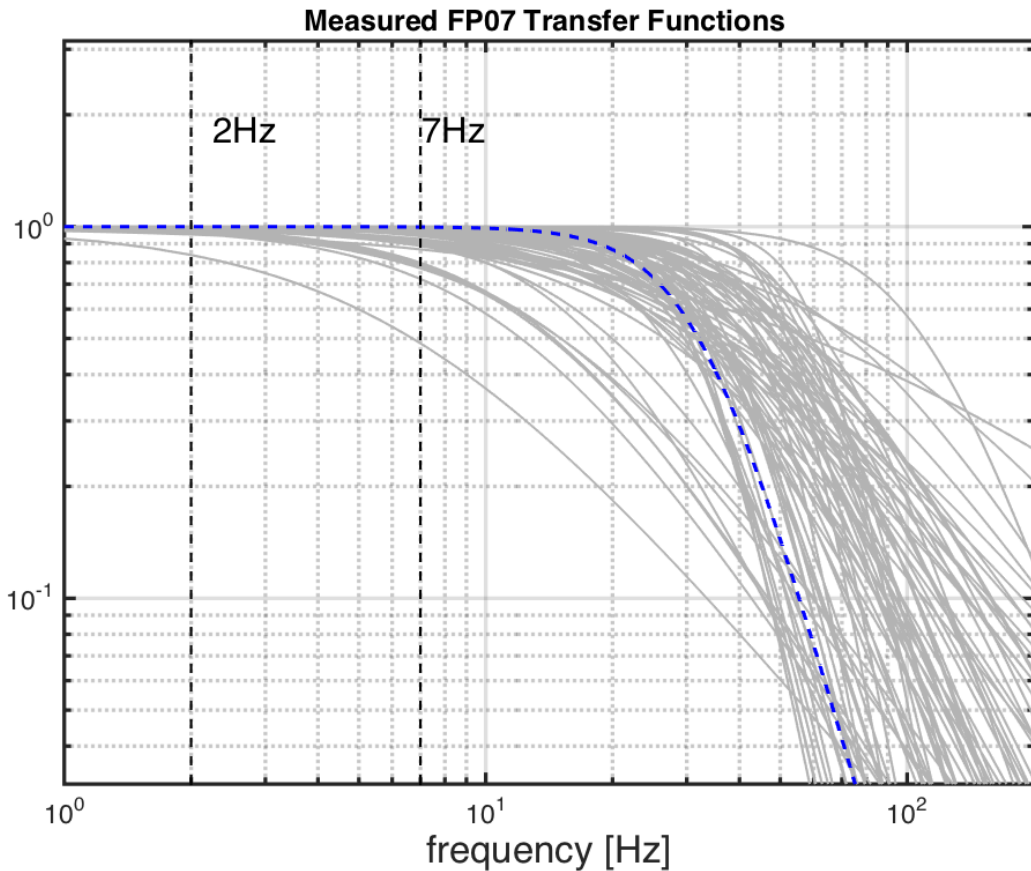
FIG. 11. Time mean of  $\chi$  for all CTD- $\chi$  pod - Chameleon cast pairs, with 95% bootstrap confidence intervals.



456 FIG. 12. Histogram of % error for  $\chi$  computed with constant added to fallspeed, in order to examine sensitivity  
 457 to fallspeed. Vertical lines indicate the mean of each distribution.



458 FIG. 13. Left: 2D histograms of  $\chi$  computed using the iterative  $\chi_{\text{pod}}$  method (top) and the MLE fit (bottom)  
 459 versus  $\chi$  computed from Chameleon. Note that the MLE method underestimates  $\chi$  at larger magnitudes. Right:  
 460 Histograms of the log of ratios for different ranges of  $\epsilon$ . The mean of each distribution is given above.



461 FIG. 14. Measured FP07 thermistor transfer functions from historical database. Vertical dashed lines show  
 462 the frequency range used in  $\chi$ pod method. Dashed blue line is a generic transfer function found to best match  
 463 measured functions.